ACS APPLIED MATERIALS & INTERFACES

Research Article

Cite This: ACS Appl. Mater. Interfaces XXXX, XXX, XXX−XXX

www.acsami.org

Controllable Preparation of Ordered and Hierarchically Buckled Structures for Inflatable Tumor Ablation, Volumetric Strain Sensor, and Communication via Inflatable Antenna

Run Wang,[†,#] Zhongsheng Liu,[†,‡,#] Guoyun Wan,[§,#] Tianjiao Jia,[†] Chao Zhang,[∥] Xuemin Wang,[△,⊥] Mei Zhang,[▽] Dong Qian,[△,⊥] Monica Jung de Andrade,[⊥] Nan Jiang,[†] Shougen Yin,[○] Rui Zhang,[△,⊥] Deqiang Feng,[†] Weichao Wang,[†] Hui Zhang,[⊥] Hong Chen,[‡] Yinsong Wang,[§] Raquel Ovalle-Robles,[◆] Kanzan Inoue,[◆] Hongbing Lu,[△,⊥] Shaoli Fang,[⊥] Ray H. Baughman,[⊥] and Zunfeng Liu*[,†]

[†]State Key Laboratory of Medicinal Chemical Biology, Key Laboratory of Functional Polymer Materials, College of Electronic Information and Optics Engineering, and College of Pharmacy, Nankai University, Tianjin 300071, China

[‡]School of Materials Science and Energy Engineering, Foshan University, Foshan, Guangdong 528000, China

[§]Tianjin Key Laboratory on Technologies Enabling Development of Clinical Therapeutics and Diagnostics (Theranostics), School of Pharmacy, Tianjin Medical University, Tianjin 300070, China

[∥]Jiangsu Key Laboratory of Bioactive Natural Product Research and State Key Laboratory of Natural Medicines, China Pharmaceutical University, Nanjing 210009, China

[△]Department of Mechanical Engineering, University of Texas at Dallas, Richardson, Texas 75080, United States

[⊥]Alan G. MacDiarmid NanoTech Institute, University of Texas at Dallas, Richardson, Texas 75080, United States

[▽]High-Performance Materials Institute, Florida State University, Tallahassee, Florida 32306, United States

[○]Key Laboratory of Display Materials and Photoelectric Devices, School of Materials Science and Engineering, Tianjin University of Technology, Tianjin 300384, China

[◆]Nano-Science and Technology Center, Lintec of America, Inc., Richardson, Texas 75081, United States

Supporting Information

ABSTRACT: Inflatable conducting devices providing improved properties and functionalities are needed for diverse applications. However, the difficult part in making high-performance inflatable devices is the enabling of two-dimensional (2D) buckles with controlled structures on inflatable catheters. Here, we report the fabrication of highly inflatable devices with controllable structures by wrapping the super-aligned carbon nanotube sheet (SACNS) on the pre-inflated catheter. The resulting structure exhibits unique 2D buckled structures including quasi-parallel buckles, crisscrossed buckles, and hierarchically buckled structures, which enables reversible structural changes of 7470% volumetric strain. The 2D SACNS buckled structures show stable electrical conductance and surface wettability during large strain inflation/deflation cycles. Inflatable devices including inflatable tumor ablation, capacitive volumetric strain sensor, and communication via inflatable radio frequency antenna based on these structures are demonstrated.

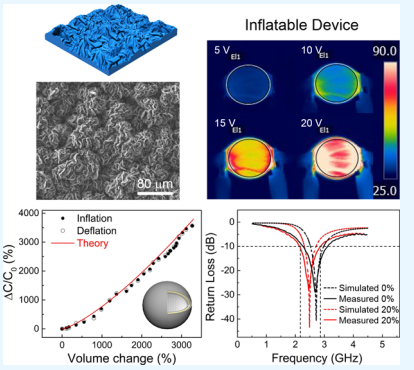

KEYWORDS: *buckled structure, carbon nanotube, inflatable tumor ablation, volumetric strain sensor, inflatable antenna*

Controllably generating variable conductive surface patterns that can handle large deformation is of great importance for designing inflatable and wearable electronics. Different types of membrane-like buckled structures are widely used in nature, which are germane to the survival and behavior of many living organisms.[1−4] In recent years, buckled structures have brought about advanced functions in design of modern materials, for example, they are becoming fundamentally important for developing stretchable and inflatable electronic devices such as artificial skin, sensors, antenna, etc.[5−11] Recently, there have been many reports on controlling the buckled morphology using different materials and structures because it can critically influence the properties of stretchable electronic materials.[12−14] A general way to produce buckled structures for stretchable electronics is to coat a thin conductive layer on a pre-stretched elastomeric substrate

Received: November 2, 2018
Accepted: February 8, 2019
Published: February 8, 2019

DOI: 10.1021/acsami.8b19241
ACS Appl. Mater. Interfaces XXXX, XXX, XXX−XXX

followed by release of the pre-strain.[15−17] When strain is released from the specimen, the mismatch between bending-dominated deformation of the conducting layer and compressing-dominated deformation of the elastic substrate causes the skin layer to buckle in response to the relaxation of the pre-strain. In this process, however, cracks are frequently formed in the metal or semiconducting layer in the lateral direction (with respect to the stretch/release direction) of the rubber fiber. This is because during stretch release of the rubber fiber (Poisson's ratio of 0.5), the length tends to decrease and the diameter and circumference tend to increase, resulting in stretching of the conducting layer to form cracks.[18] The cracking in the conducting layer during buckle formation has been a great challenge for the fabrication of stretchable and inflatable electronic devices.

This lateral crack problem can be circumvented by using 2D buckled structures that are highly stretchable and tunable with good reversibility. These structures can be formed in both x and y directions on the surface without crack formation via 2D compressive strain, thereby allowing both one-dimensional stretching and two-dimensional stretching. It is always observed that the uniaxial compressive force can generate parallel buckles in one dimension, while labyrinthine morphologies are always generated in thin films on compliant substrates under two-dimensional compressive deformation.[19−21] In fact, it is always difficult to control the surface buckling patterns in such cases because of the uncontrollable local stress distribution in the deformed surface. However, controlling the morphology of the buckled structures is of great importance in a number of fields with diverse applications, such as diffraction gratings, microfluidic devices, microelectronics, photonic materials, sensors, and tunable hydrophilic surfaces. Different methods have been developed to prepare ordered structures via small strain compression, such as dewetting of liquid polymer films,[22,23] phase separation of polymer blends or block copolymers,[24] deposition of thin layer on hot substrates followed by cooling, such as coating metal or semiconducting thin film or creating a hard surface layer by ultraviolet/ozone treatment.[25−28] However, these ordered buckled structures can only handle deformation in a very small strain range, and many of these approaches can only take advantage of nonconducting materials for surface coating. It is highly desirable to develop a method that can controllably generate variable surface patterns that can handle large deformation in order to meet the requirements in applications that call for high expandability.

Among the abovementioned methods, engineering the substrate pattern has been shown to be an effective way to control the stress field distribution and generate ordered two-dimensional buckles in the surface layer.[29] Another possible strategy is to engineer the stress field distribution in the surface conductive layer. The super-aligned carbon nanotube sheet (SACNS) is an anisotropic conductive material,[30,31] in which the carbon nanotubes self-assemble to form aligned structures. The SACNS show anisotropic mechanical properties, with higher mechanical strength in the carbon nanotube (CNT) alignment direction than that in the transverse direction. Moreover, the SACNS show strong adhesion with elastomeric substrates via van der Waals interaction, which has been used as the conductive layer to generate one-dimensional buckled structures for fabricating stretchable electronic devices by us and other research groups.[5,14,32−37] Currently, there are no published reports on fabrication and characterization of buckled structures made of anisotropic materials via loading conditions other than uniaxial compression (i.e., omnidirectional compression). From both theoretical perspective and application perspective, understanding the buckling behavior of anisotropic conducting materials subjected to omnidirectional compression and how they would be affected by the substrate morphology are critically important in the design and fabrication of multifunctional inflatable devices.

In this paper, we report controllable fabrication of ordered 2D buckled structures using SACNS (including quasi-parallel buckles and crisscrossed buckles) and multiscale hierarchically buckled structures. We first prepared quasi-parallel buckles and crisscrossed buckles by controlling the stacking orientation of the SACNS. Briefly, these buckled structures were prepared by the following steps. First, an elastomeric catheter was inflated, and the SACNSs were attached on the surface of the pre-inflated elastomeric catheter and condensed on the catheter surface by using ethanol. After deflation of the catheter, controllable quasi-parallel buckles of SACNS were formed. By replacing one piece of SACNS with two pieces of perpendicularly stacked SACNS, the crisscrossed buckled structures were prepared. When the lateral expansion degree of the catheter was beyond a certain strain (220% in this case), island-shaped structures were observed on the catheter surface. By using this catheter with island-shaped surface, different types of multiscale hierarchically buckled structures of SACNS were formed. This method demonstrated a novel and simple approach that can controllably generate different types of buckled structures including ordered two-dimensional patterns and variable types of hierarchically buckled structures. These SACNS patterns can reach 100% surface coverage for both deflated and inflated catheters, which was suitable for applications requiring a high coverage of electrodes.

In recent studies, the incorporation of two-dimensional hierarchically buckled structures in gold, graphene, and carbon nanotube thin films has enabled mechanically robust thin-film actuators, elastic conductors, tunable hydrophobic surfaces, energy storage devices, and cell culturing surfaces.[8,9,21,38] These examples convincingly demonstrated that devices with the desired properties can be successfully constructed on stretchable surfaces. To the best of our knowledge, inflatable electronic devices such as inflatable tumor ablation, antenna, and capacitive volumetric sensors enabled by the incorporation of 2D buckles with controlled structures have not yet been explored.[4,6−9] In fact, these inflatable devices may find very important applications in healthcare, wireless communications, and sensing. For example, in minimally invasive surgery, a deflated catheter is introduced from an incision to reach the difficult-to-reach diseased intravascular and endocardial regions or the cavity of the body,[39] and they can seamlessly integrate with human organs after inflation. As such, a more accurate diagnosis and more complete treatment can be realized. The catheter size or volume can be measured using an inflatable capacitive strain/volumetric sensor, and the signals can be wirelessly transmitted via an inflatable antenna, both of which could be assembled on the inflatable catheter. In this paper, the as-prepared inflatable conductors made of two-dimensional buckled SACNS showed highly stable electrical properties (7.8% resistance change for $SACNS_{10}$/catheter over 330% strain increase in omnidirections, corresponding to 7470% volume change). These inflatable conductors showed tunable surface wetting properties. Inflatable devices such as inflatable

DOI: 10.1021/acsami.8b19241
ACS Appl. Mater. Interfaces XXXX, XXX, XXX−XXX

tumor ablation, inflatable capacitive volumetric sensor, and inflatable radio frequency (RF) antenna were demonstrated.

We use an anisotropic SACNS material as the conducting layer on inflatable devices and enable additional functions by including other rubber and SACNS layers. The SACNS sheets used in this study are drawn from a multiwalled carbon nanotube (MWNT) forest of ~250 μm in height and ~9 nm in diameter, which is a self-aligned anisotropic conducting material, with higher mechanical strength in the carbon nanotube (CNT) alignment direction than that in the transverse direction.[30,31] To make inflatable conducting devices, stacks of the SACNSs were deposited on the pre-inflated catheter surface, densified with ethanol, and deflated to the unstrained state to generate the buckled structures of SACNS, which is denoted as SACNS$_m$/catheter hereafter, where m denotes the number of the SACNS layers (Figure 1A). After ethanol densification, the SACNS layers showed strong adhesion with elastomeric substrates via van der Waals interaction. We first prepared quasi-parallel buckles and crisscrossed buckles by controlling the stacking orientation of the SACNS layers. Briefly, quasi-parallel buckles were prepared by attaching one layer of SACNS on the surface of a pre-inflated elastomeric catheter followed by deflation (Figure 1C).

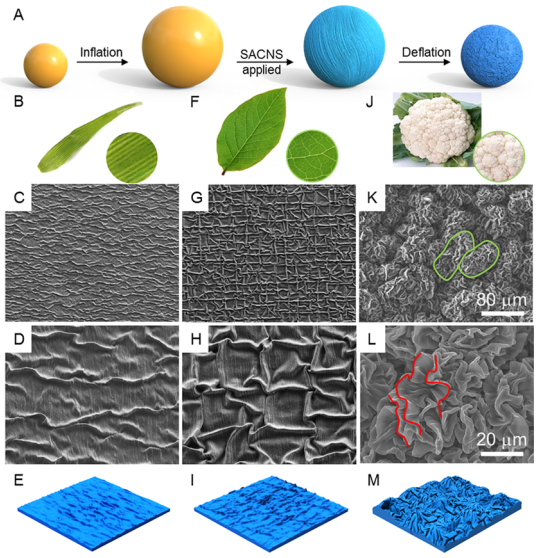

Figure 1. (A) Fabrication steps of a SACNS$_m$/catheter, where the catheter was omnidirectionally inflated. (B, F, J) Photographs of plant leaves for demonstrating the patterns of different types of buckled structures: (B) parallel buckles, (F) crisscrossed buckles, and (J) hierarchical buckles. (C–E) SEM images of (C) low magnification and (D) high magnification of the SACNS$_5$/catheter and (E) schematic demonstration of the quasi-parallel buckled structure. The alignment direction of carbon nanotubes is vertical. (G–I) SEM images of (G) low magnification and (H) high magnification of the SACNS$_5$/catheter and (I) schematic demonstration of the criss-crossed buckles prepared from the overlap of vertically and horizontally aligned carbon nanotubes. The biaxial omnidirectional fabrication strain was 13% for (C), (D), (G), and (H). (K–M) SEM images of (K) low magnification and (L) high magnification of the SACNS$_5$/catheter and (M) schematic demonstration of the hierarchically buckled structure. The alignment direction of carbon nanotubes is vertical. The biaxial omnidirectional fabrication strain was 430% for (K) and (L). The green circles in (K) demonstrated the second-order ravines, and the red curves in (L) demonstrated the first-order buckles.

By replacing one layer of SACNS by two perpendicularly-stacked layers of SACNSs, crisscrossed buckled structures were observed (Figure 1G). When the lateral expansion of the catheter was beyond a certain strain (220% in this case), long island-shaped structures with multiscale hierarchically buckled structures of SACNS were observed on the catheter surface (Figure 1K). Such different types of buckled structures are widely found in nature, as shown in Figure 1B,F,J. By using this catheter with the island-shaped surface, different types of multiscale hierarchically buckled structures of SACNS formed. Using this approach, we demonstrated a novel and simple way to control the resulting buckled SACNS structures including ordered two-dimensional patterns and various types of hierarchically buckled structures. These SACNS structures can cover the whole surface for both deflated and inflated catheters, which enable applications requiring a high coverage of electrodes.

To understand the properties of the buckled SACNS structures, we define the biaxial omnidirectional strains of the SACNS$_m$/catheter as ε_1 and ε_2, which represents the percent change in length over the undeformed length along the two orthogonal biaxial omnidirections during catheter inflation. $\varepsilon_1 = (l_1 - l_0)/l_0$, $\varepsilon_2 = (l_2 - l_0)/l_0$, where l_1 and l_2 are the deformed lengths and l_0 is the undeformed length along the orthogonal biaxial omnidirections. The fabrication strains in biaxial omnidirections of the SACNS$_m$/catheter are defined as ε_{fab1} and ε_{fab2}. If not specified, the catheter used in this paper was spherical so that ε_1 can be considered to be equal to ε_2 (denoted as ε); ε_{fab1} can be considered to be equal to ε_{fab2} (denoted as ε_{fab}). Due to plastic deformation after deposition of SACNS on the inflated catheter, the maximum available strain (ε_{max}) was smaller than the fabrication strain.[40] Correspondingly, the volumetirc strain (ε_V) of the SACNS$_m$/catheter is the percent volume change, $(V_1 - V_0)/V_0$, where V_1 and V_0 are the catheter volumes at ε_1 and ε_0, respectively. It should be noted that the carbon nanotube sheets are rectangular and the inflated catheter are spherical; there must be some overlap of the SACNS in some areas if the surface is fully covered with the SACNS. Therefore, uniform coating of the SACNS on the catheter surface can be obtained in a limited surface area, and we take this area for surface structural analysis in the following experiments. Moreover, it is noted that the area that is to the other side of the gas charging valve is investigated because the stress distribution in the area close to the gas charging valve is not uniform.

Microstructural and electrical resistance characterizations were conducted for the partially covered SACNS$_m$/catheters after preconditioning it through five cycles of inflation/deflation to the maximum strain prior to plastic stretch of SACNS layers in the nanotube alignment direction. During sequential inflation/deflation cycles, the dependence of structure on strain was reversibly retained, and no observable delamination occurred (Figure S1). When applying a small fabrication strain (ε_{fab} = 13%) and applying five layers of unidirectionally stacked SACNS on an inflated catheter surface, the quasi-paralleled buckled structure of SACNS was observed as shown in Figure 1C. Even though the SACNS layers were omnidirectionally compressed, the resulting buckles are generally oriented in the direction perpendicular to the CNT alignment direction (Figure 1D). Figure 1E shows a schematic illustration of quasi-parallel buckled structures. In addition, tiny wrinkles were also observed in the orientation perpendicular to the relatively large buckles. Previous reports

DOI: 10.1021/acsami.8b19241
ACS Appl. Mater. Interfaces XXXX, XXX, XXX–XXX

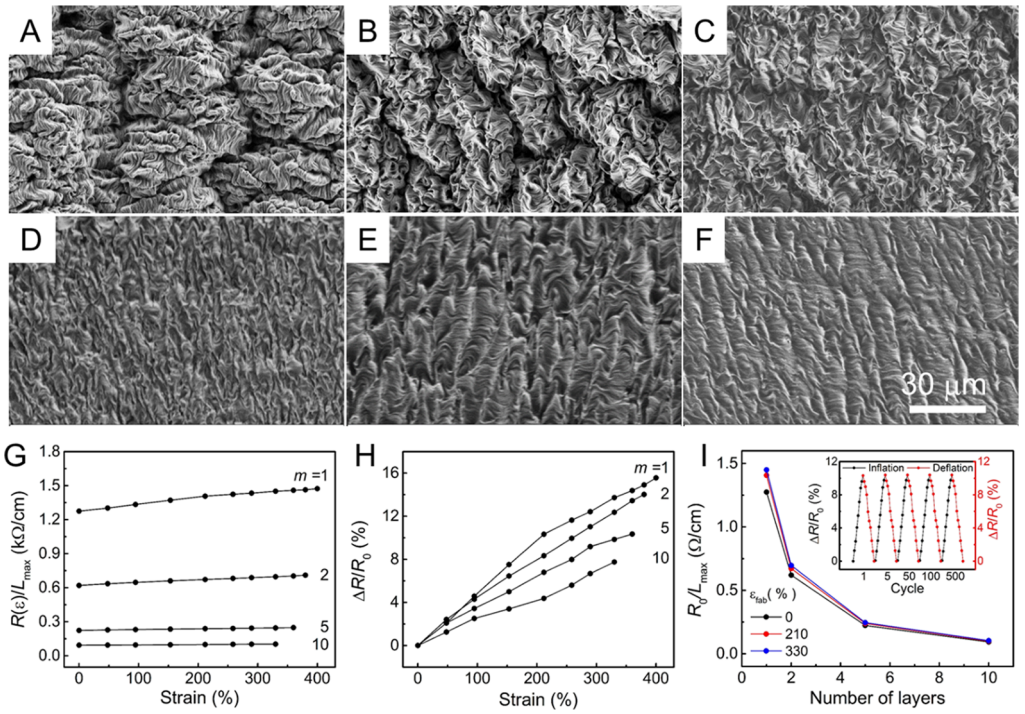

Figure 2. (A–F) SEM images showing the evolution of the buckled structure for a SACNS$_5$/catheter (ε_{fab} = 450%) during the biaxial stretch. The strains are 0, 20, 50, 100, 200, and 300% for (A) to (F), respectively. (G–I) Electrical properties of SACNS$_m$/catheters. (G) Length-normalized resistance as a function of strain for SACNS$_m$/catheters with different m. (H) Percent resistance change as a function of strain for SACNS$_m$/catheters. (I) Length-normalized resistance as a function of m for SACNS$_m$/catheters at different strains. Inset shows percent resistance change for a SACNS$_5$/catheter during inflation/deflation cycles.

show that buckling profiles were largely dependent on the mechanical properties of the surface coating layer,[41] and thus, this anisotropic buckled structure observed for our SACNS$_m$/catheter was a result of the highly anisotropic mechanical properties of the SACNS layers, which had much higher Young's modulus in the nanotube direction compared to that in the transversal direction.[30] This 2D quasi-parallel buckled structure of SACNS layers is different from previously reported one-dimensional (1D) buckled structures prepared using uniaxial compression (Figure S2).[5,14,32−37] In those reports, the CNT sheets were uniaxially compressed in the nanotube alignment direction forming 1D parallel buckles perpendicular to the stretch-release direction, and periodic necking was observed on the ridge of the buckles due to the lateral expansion during length contraction because the rubber substrate has a Poisson's ratio of 0.5 (volume conservation during deformation),[5,14,34] as shown in Figure S3. The mechanical property of the spherical catheter substrate was also shown in Figure S4.

When increasing fabrication strains from 17 to 150%, the increased omnidirectional compression pressure forced the quasi-paralleled buckles to get denser, and the orientation of SACNS buckles deteriorated (Figure S5A–D). Further increasing the fabrication strain to 220%, hierarchically buckled structures were observed (Figure S5E), where densely packed, wavy short-period SACNS buckles (buckle width of ∼1 μm; denoted as buckles in the following discussions) formed on top of long islands with varying lengths and widths of several tens of micrometers (denoted as islands in the following discussions). Figure 1K,L shows the low- and high-magnification SEM images for the hierarchically buckled structure of a SACNS$_5$/catheter for 430% fabrication strain. Figure 1M shows a schematic illustration of superposition of SACNS buckles on islands. The islands indicated in green circles (Figure 1K) show an average width of ∼25 μm. Figure 1L shows the magnified structure of the wavy SACNS buckles on top of an island, where CNT alignment in the buckle is perpendicular to the buckle ridge. The hierarchically buckled structures consist of over several order of micro/nanoscales from several tens of micrometers for the islands, to micrometers for the SACNS buckles, and to nanometer sizes for carbon nanotube bundles. These hierarchically buckled structures appeared to be the most favorable structures for large fabrication strains from 220 to 456% (Figure S5E–I). The average width of the buckles is ∼1.2 μm for fabrication strains below 360% and decreases to 0.8 μm with fabrication strains increasing from 360 to 456%. The average widths of the islands are in the range of 20 to 25 μm for fabrication strains from 220 to 456% (Figure S6). These unique buckling structures not only promote high surface roughness but also led to high density of CNT in a nonstretched projected area. Such special features could be valuable for multifunctional applications that would require tunability of hydrophobicity and transmittance of conducting surface layer, especially with full coverage.

Figure 2A–F shows the reversible structure evolution of the buckled structure for a SACNS$_5$/catheter (ε_{fab} = 450%) during a biaxial stretch from 0 to 300% strain. For biaxial strains of 0 and 20% (Figure 2A,B), the hierarchically buckled structures of SACNS buckles and islands are easily identified. As the biaxial strain increased to 50%, the island structure becomes less pronounced (Figure 2C). The island structure completely disappears at a biaxial strain of 100%, and the SACNS buckles become parallel to each other, which are perpendicular to the

DOI: 10.1021/acsami.8b19241
ACS Appl. Mater. Interfaces XXXX, XXX, XXX−XXX

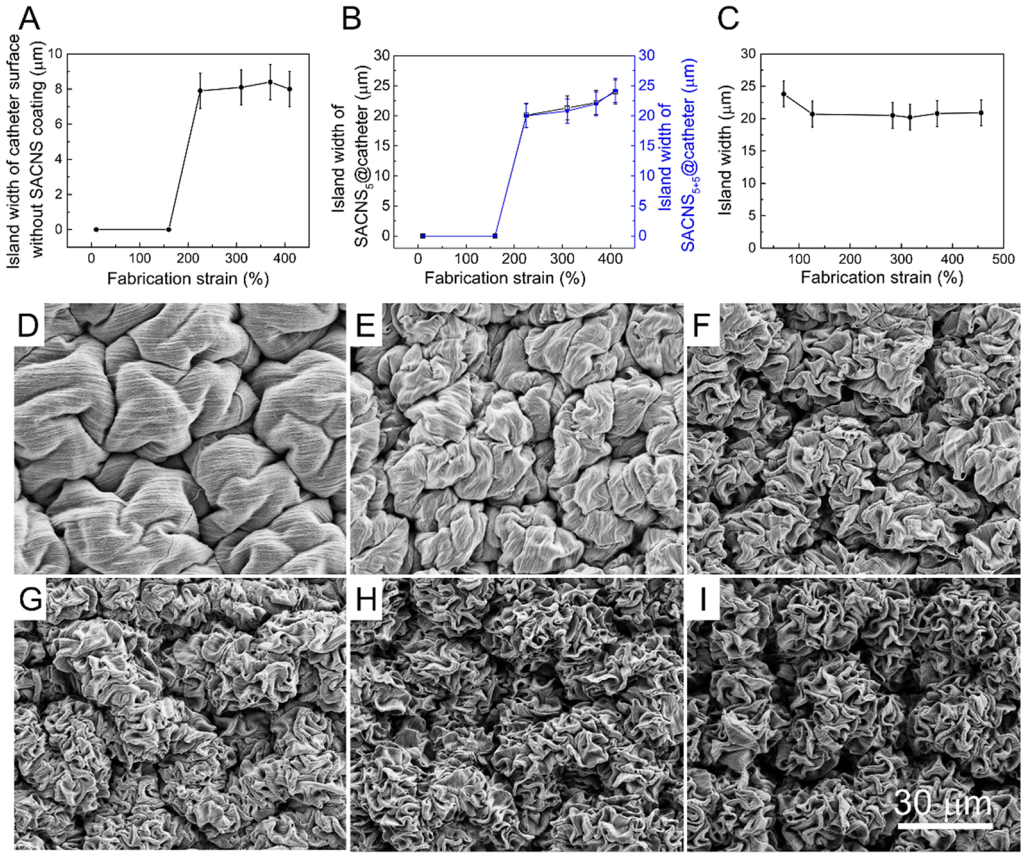

Figure 3. (A, B) Average widths as a function of fabrication strain for (A) islands without SACNS coating and (B) the $SACNS_5$/catheter and $SACNS_{5+5}$/catheter, which were derived from Figure S8A−F. (C) Average width of islands as a function of fabrication strain for $SACNS_5$/catheters. The data were derived from (D) to (I). The irregular edges due to fabrication imperfections were not used for calculation of average buckle width. (D−I) SEM images of $SACNS_5$/catheters prepared on a pre-inflated catheter surface with one inflation/deflation cycle to 456% strain. The fabrication strains for SACNS coating were 70, 126, 283, 317, 370, and 456% for (D) to (I), respectively.

alignment direction of the carbon nanotube bundles (Figure 2D). Further increasing the biaxial strains to 200 and 300%, SACNS buckles become more separated and less visible (Figure 2E,F). As the biaxial strain increases from 0 to 300%, the separation between buckles increases gradually from 1.0 to 2.6 μm. The average width of the islands decreases from 25 to 12 μm for fabrication strains from 0 to 50% (Figure S7).

When two stacks of $SACNS_5$ were orthogonally stacked on a pre-inflated elastomer surface (ε_{fab} = 13%), a crisscrossed buckled structure was observed after catheter deflation (Figure 1G−I). These crisscrossed buckles were formed from a combination of the independent buckling of each orthogonally stacked $SACNS_5$ in perpendicular directions. SACNS is an anisotropic material, and its Young's modulus in one direction is much higher than that in the transverse direction.[30] It is reported that critical strain for buckle formation increases when the Young's modulus ratio of film to substrate decreases.[42−46] For a fabrication strain of 13%, buckles were formed along the nanotube direction because it reached the critical strain for SACNS in the direction having a higher Young's modulus. While in the weak Young's modulus direction (perpendicular to the nanotube direction), fabrication strain was less than the critical strain; therefore, no buckles formed. When the same number of SACNS was stacked in both directions, crisscrossed buckles of SACNS formed since the critical strain was reached in both directions due to comparable Young's modulus. As the fabrication strain increased to 430%, which was much higher than the critical strain, the resulting wrinkle pattern became disordered as shown in Figure 1K.

To understand the formation mechanism of the hierarchically buckled SACNS structures in Figure 1K,L, we characterized the surface morphology of a catheter with and without SACNS coating for different fabrication strains. Figure S8A−F shows that two pieces of $SACNS_5$ layers were stacked orthogonally to each other, where the top left corners of the images show the catheter surface without SACNS. The images show quasi-periodic structures except for the edge of the SACNS, which should be ascribed to the manufacturing imperfections. For fabrication strains from 10 to 160%, only short-period SACNS buckles were observed, and no plastic deformation on the catheter surface was observed in the area without SACNS coating, as shown in Figure S8A,B. For fabrication strains from 225 to 410%, hierarchically buckled structures were observed in the areas covered with either unidirectional $SACNS_5$ or two perpendicularly stacked $SACNS_5$ (denoted as $SACNS_{5+5}$/catheter in the following discussions), as shown in Figure S8C−F. There is no significant difference between the average island width for $SACNS_5$/catheter and that for $SACNS_{5+5}$/catheter, which increases with increasing fabrication strain (Figure 3B). Interestingly, for high fabrication strains (225 to 410%), micrometer-scale islands were also observed on the catheter surface without SACNS coating (Figure S8C−F), indicating

DOI: 10.1021/acsami.8b19241
ACS Appl. Mater. Interfaces XXXX, XXX, XXX−XXX

that the formation of these islands is due to the plastic deformation of the catheter surface. The average island width (~20 μm) for $SACNS_{5+5}$/catheter (with 225% fabrication strain) is significantly larger (~8.5 μm) than that for the catheter surface without SACNS coating (Figure 3A,B), which is due to modulus increase of the catheter surface after SACNS coating.[16]

The relationship between the number of SACNS layer and the island width of $SACNS_m$/catheter was investigated by characterizing buckling morphology of $SACNS_m$/catheters having different number of layers of SACNS. Figure S9 shows the SEM images of $SACNS_m$/catheter for m = 1 to 10 for a fabrication strain of 456%, and Figure S10 shows the average widths of SACNS buckles and islands. The average widths of the SACNS buckles were 0.3, 0.5, 0.8, and 1.0 μm for m = 1, 2, 5, and 10, respectively, and the average widths of the islands were 16, 21, 25, and 28 μm for m = 1, 2, 5, and 10, respectively. It was observed that the increase of SACNS thickness increases the widths of both SACNS buckles and islands.

In order to generate islands on the catheter surface, the catheter is pre-inflated (from 70 to 456% strain) with one prior inflation/deflation cycle to 456% strain, followed by coating with unidirectional $SACNS_5$. All tested fabrication strains yielded island structures, as shown in Figure 3D−I. For a fabrication strain of 70%, no SACNS buckles were observed on the islands. This behavior was quite different from the buckled structure of SACNS prepared on a flat catheter surface without pre-existing islands, where the SACNS buckled structure was observed for a fabrication strain as low as 10% (Figure S1A). As fabrication strain increased up to 456%, short-period SACNS buckles were observed on the islands. The island width was ~24 μm for a fabrication strain of 70% then decreased to ~20 μm as the fabrication strain increased to 456% as shown in Figure 3C. An interesting observation is that buckle density increased significantly from ~175/mm to ~300/mm as fabrication strain increased from 283 to 456%. The tunable buckle density with compressive strains is also reported.[5,6,14]

Considering that large available strains are preferred for inflatable electronic devices, the hierarchically buckled structure ($SACNS_5$/catheter) shown in Figure 1K was used for further investigations of the electrical and surface wetting properties. Figure 2G shows electrical resistance $(R(\varepsilon)/L_{max})$ as a function of strain (ε) for $SACNS_m$/catheters, where $R(\varepsilon)$ is the SACNS resistance at the strain (ε) along the nanotube direction having a maximum stretched length (L_{max}), which is equal to the length at the fabrication strain. Figure 2H shows strain dependence of percent resistance change $(\Delta R(\varepsilon)/R_0)$ for $SACNS_m$/catheters (from 0 to 330% strain), where $\Delta R(\varepsilon) = R(\varepsilon) - R_0$ and R_0 is $R(0)$. These results show that percent resistance change decreases with increasing m (from 13.7% for m = 1 to 7.8% for m = 10). To our knowledge, there is no available literature data of resistance change for 2D stretchable conductors during biaxial stretching or during inflation; the percent resistance changes for our $SACNS_m$/catheters are among the lowest level compared with those previously reported pioneering work for other types of elastomeric conductors over uniaxial stretching, such as 2D graphene buckled structures from Zhao's group (80% resistance change for 450% uniaxial strain),[8] 2D curved structure of carbon nanotube films from Bao's group (60% resistance change for 200% strain),[47] graphene network from Cheng's group (200% resistance change for 90% uniaxial strain),[48] hierarchically buckled carbon nanotube films of our previous work (<5% resistance change for over 1000% uniaxial strain),[5] and hierarchically buckled graphene film from Wang's group (5.9% resistance change for 400% uniaxial strain).[38] Figure 2I shows that R_0/L_{max} for $SACNS_m$/catheters decreases with increasing m (1.27, 0.61, 0.22, and 0.09 kΩ cm^{-1} for m = 1, 2, 5, and 10) and only slightly increases with increasing fabrication strain. Moreover, the resistance change for $SACNS_5$/catheters over a 260% strain range varied slightly during 500 inflation/deflation cycles (Figure 2I, inset). Because of this stable resistance and interface over large inflation, the $SACNS_m$/catheter could be a promising candidate for inflatable electronics for many potential applications such as tumor ablation, capacitive volumetric sensor, and RF antenna.[49−52]

In addition to electrical properties, we also studied the surface hydrophobicity of $SACNS_m$/catheter during the biaxial stretch. One piece of the composite film was cut from the $SACNS_m$/catheter, and it was biaxially stretched to measure the contact angle. Figure S11 demonstrates the water contact angle changing from 145° to 110° for a water droplet placed on top of the $SACNS_{10}$/catheter. These tunable hydrophobic properties were not observed on the surfaces of pristine catheters with and without secondary ravines, indicating that the formation of the hierarchically buckled SACNS structure was responsible for the tunable hydrophobic surface properties of the $SACNS_{10}$/catheter. The tunable hydrophobic properties at different inflation strains would help changing the wetting with liquid by changing the strain. For example, it can be used to have good contact with water or body fluid when expanded and easily be cleaned when deflated by forming buckles.

Another potential application for $SACNS_m$/catheters is inflatable tumor ablation. Pioneering works by Rogers's and Huang's group about two-dimensional stretchable conducting devices use thin metallic or semiconductor films having micropatterned networks, buckles, or serpentine-like structures to enable biaxial stretchability.[53,54] These structures can provide partial coverage of the conducting surface at an inflated state. For applications such as tumor ablation, complete coverage of the conducting surface for an inflated catheter is preferred because of the requirement of uniform heating. Here, for demonstration purposes, we used a tubular catheter as the inflatable substrate. By completely coating the $SACNS_5$ layer on an inflated tubular catheter, we were able to prepare a tubular $SACNS_5$/catheter having complete SACNS coverage of the entire catheter outer surface. The volume fabrication strain (ε_{vfab}) is defined as $\varepsilon_{vfab} = (V_{fab} - V_0)/V_0$, where V_{fab} is the volume of the inflated catheter for coating SACNS and V_0 is the volume of the nonstrained catheter. Here, ε_{vfab} was 1100%, and an electrical resistance of 168 Ω along the tube direction was obtained in the inflated state, which could reach up to 1000% volume increase. Figure S12 shows the SEM images for the hierarchically buckled structure of a tubular $SACNS_5$/catheter for 1100% volume fabrication strain. Repeated inflation/deflation cycles did not cause delamination of the SACNS layer from the catheter surface, and the resistance remained stable as shown in Figure 4A, suitable for inflatable tumor ablation devices. Figure 4B shows infrared (IR) images of a tubular $SACNS_5$/catheter in the inflated state when different direct current (DC) voltages were applied (Movie S1). The temperature at different positions of the catheter surface should be different because the SACNSs

DOI: 10.1021/acsami.8b19241
ACS Appl. Mater. Interfaces XXXX, XXX, XXX−XXX

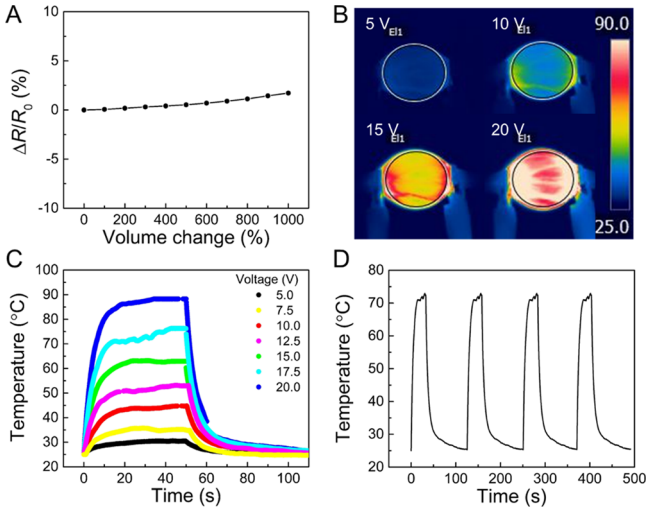

Figure 4. (A) Percentage of resistance change as a function of the volumetric strain of the tubular $SACNS_5$/catheter for tumor ablation. (B) Infrared images of the tubular $SACNS_5$/catheter during electro-heating with different applied different voltages after inflation. (C) Temperature as a function of time of the tubular $SACNS_5$/catheter at different applied voltages. (D) Temperature as a function of time of the tubular $SACNS_5$/catheter during four cycles of electro-heating and cooling by switching on/off at 17.5 V (0.10 W/cm^2). The volume fabrication strain is 1100%.

are not uniformly coated on the catheter surface, and therefore, the average temperature was obtained using the IR camera. When voltage was applied, the surface temperature of the tubular $SACNS_5$/catheter reached a plateau in less than 10 s (Figure 4C). The average plateau temperature of the tubular $SACNS_5$/catheter surface increased from 30.0 to 87.0 °C as the applied voltage increased from 5.0 to 20.0 V (0.008 to 0.13 W/cm^2), which is high enough for tumor ablation applications such as burning infected tissues, exsanguination prevention, or cancerous tumor removal. When applied voltage was turned off, the $SACNS_5$/catheter cooled down to room temperature in less than 10 s. Figure 4D shows the surface temperature as a function of time for the tubular $SACNS_5$/catheter during two cycles of electro-heating and cooling by switching on/off at 17.5 V (0.10 W/cm^2). This technology could be beneficial for minimally invasive surgical applications for irregular surfaces of human body organs by the application-specific design of the structure and shape of the conducting catheter.

Cancer has become the first killer of human lives, and the way to treat cancers perplexes most medical scientists. Hyperthermic tumor therapy has gradually become an important therapeutic method in clinical practice due to the thermolabile peculiarity of cancer cells.[55] High-intensity focused ultrasound[56,57] and photothermal therapy (PTT)[58,59] are the two most widely studied ways of hyperthermic tumor therapy. In this paper, the fact that the $SACNS_m$/catheter acts as an effective inflatable tumor ablation electrode encouraged us to apply this electrode for thermal ablation of tumors. The toxicity assessments of SACNS found no biological safety problem, as shown in Table S1. The in vivo thermal effects of $SACNS_5$/catheter on tumor growth were evaluated in Hepa1-6 tumor-bearing mice. As shown in Figure 5A, the size of $SACNS_5$/catheter was controllable for adapting to the tumors. The $SACNS_5$/catheter can be rapidly heated to 85.0 °C in 3 min after switching on the electricity at 20.0 V (Figure 5B). Figure 5C shows that the tumor temperature is 57.5 °C at 10 min after the treatment, which is close to the heating effect in

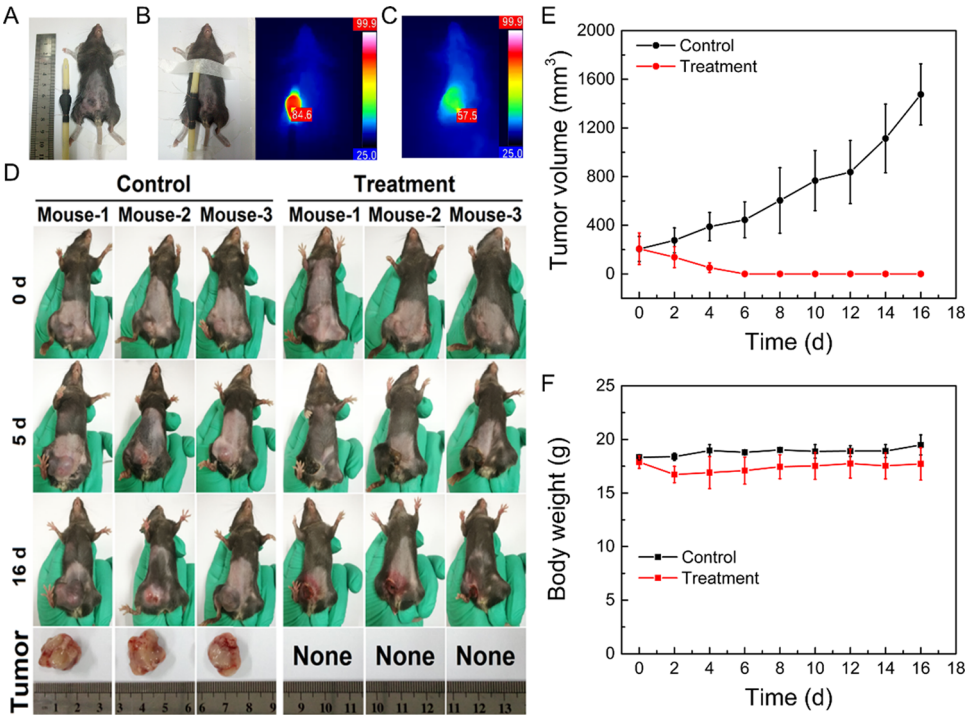

Figure 5. Application of $SACNS_m$/catheter on tumor ablation by electro-heating. (A) Dimensional image of $SACNS_5$/catheter and Hepa1-6 tumor in vivo. (B) Optical image (left) and thermal image (right) of $SACNS_5$/catheter at 3 min during the treatment progress. (C) Thermal image of the tumor 10 min after electro-heating through the $SACNS_5$/catheter. (D) Photos of mice and excised tumors during the period of electrical heating treatment. (E) Tumor growth curves and (F) body weight changes of mice in the control and treatment groups (mean ± SD, n = 3).

DOI: 10.1021/acsami.8b19241
ACS Appl. Mater. Interfaces XXXX, XXX, XXX−XXX

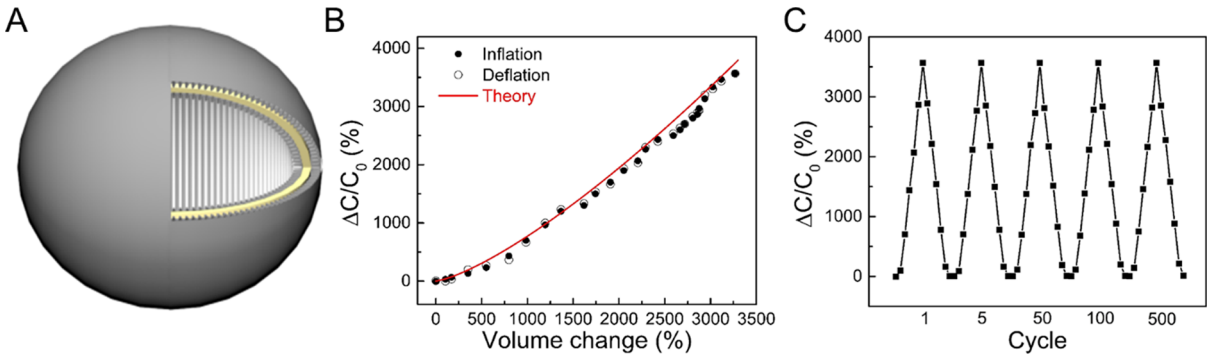

Figure 6. (A) Schematic illustration of a $SACNS_2$/catheter/$SACNS_2$ capacitor, where the inside and outside surfaces of the catheter were covered with $SACNS_2$. (B) Percent capacitance change as a function of the volumetric strain of $SACNS_2$/catheter/$SACNS_2$. (C) Percent capacitance change as a function of volumetric strain at different cycles for a $SACNS_2$/catheter/$SACNS_2$ capacitor. The omnidirectional fabrication strain is 260%.

the PTT[72]. It is worth mentioning that the $SACNS_5$/catheter still showed excellent thermal performance and maintains the temperature at 85.0 °C after heating for 30 min (data not shown). Figure 5D,E shows the effect of tumor thermal ablation during the period of 16 days after the treatment. Meanwhile, the body weights of mice were monitored after the initial treatment. As shown in Figure 5F, all mice displayed only a slight decrease in body weights, suggesting the biosafety of this electro-heating treatment based on the $SACNS_m$/catheter.

Real-time parameter feedback such as the volume of inflatable devices during inflation is important, especially for locations where imaging technologies are not applicable. Therefore, an integrated volumetirc sensor is desired for inflatable devices. Here, we demonstrate a dielectric capacitive volumetric sensor based on the $SACNS_m$/catheter. Instead of coating SACNS on the outer surface of an inflated catheter, both inner and outer surfaces of a catheter were coated by SACNS layers (ε_{fab} = 240%), which is denoted as $SACNS_m$/catheter/$SACNS_m$ in the following discussions.[54] In this structure, the catheter layer acted as a dielectric material between the SACNS layers (Figure 6A). During inflation of catheter, the catheter volume increased, and the catheter thickness became smaller, increasing the capacitance. Figure 6B shows the percent capacitance change as a function of percent volume change for $SACNS_2$/catheter/$SACNS_2$. The percent capacitance change increased monotonically by 3570% as volume increase by 3270% with high reversibility and without hysteresis.

The relationship between volume and capacitance changes for a concentric spherical conductor can be theoretically expressed as (see Section S2, Supporting Information for details)

$$\Delta C/C_0 = (V/V_0)^{4/3} - 1 \quad (1)$$

Equation 1 shows that $\Delta C/C_0$ is proportional to $(V/V_0)^{4/3}$. This theoretical prediction agreed well with our experimental results as shown in Figure 6B. As shown in Figure 6C, the percent capacitance change ($\Delta C/C_0$) for $SACNS_2$/catheter/$SACNS_2$ is highly reversible for over 500 inflation/deflation cycles. Such highly robust SACNS capacitive volumetric sensor would enable better integration with inflatable devices compared with conventional electrode materials such as carbon grease or silver paste. This nearly linear behavior of capacitance change with large volumetric strain provides a convenient way for diverse applications. A possible use of such a strain sensor may be in the case that is not linked with a rope or tube, such as a hot air balloon. Particularly, if the catheter is not uniformly inflated, then several capacitive strain sensors positioned at different places of the catheter would give more accurate information about the shape and volume of the catheter. This is different from an indeflator, which measures the pressure and amount of air indirectly via a tube and gives an estimation of the total volume.

Inflatable antennas for communications are of great importance for space exploration and medical applications. Traditional metal conductors provide excellent electrical properties for antennas, but they cannot endure large deformation and have delamination issues during inflation/deflation cycles. Considering the stable conductance over a large strain range for our $SACNS_m$/catheter, we were encouraged to construct an inflatable RF antenna. As a proof of concept, we fabricated a monopole antenna that showed a resonant frequency close to 2.45 GHz based on the inflated conductor. This frequency was in the range of commonly used Wi-Fi frequency for data communication. To improve the conductivity of SACNS, a thin layer of silver was deposited onto individual carbon nanotube bundles in SACNS using magnetron sputter deposition, which is denoted as Ag_t-SACNS, where t is the thickness of the silver layer. Similar to $SACNS_m$/catheter, a monopole antenna was fabricated by attaching one layer of $Ag_{24\ nm}$-SACNS on a pre-inflated catheter at a fabrication strain of 80%, which is denoted as $Ag_{24\ nm}$-$SACNS_1$/catheter antenna (Figure 7A).

Antenna performance was characterized by measuring the return loss (RL) for different strains and during inflation/deflation cycles. The return loss is a parameter that can be used to indicate the amount of power loss of the input signal. The RL in decibels (dB) can be expressed by eq 2

$$RL = 10 \log_{10}(P_r/P_i) \quad (2)$$

where P_r is the reflected power and P_i is the incident power.

Figure 7B shows the measured and simulated return loss for a $Ag_{24\ nm}$-$SACNS_1$/catheter antenna at 0 and 20% strain. For the frequency range between 500 MHz to 4.5 GHz, the measured resonant frequency is 2.66 GHz, which is very close to the simulation result of 2.72 GHz. The measured peak return loss is −28.4 dB, corresponding to efficient transmission of over 99.86% power at the resonant frequency. As the antenna is inflated to 20% strain, the measured resonant

DOI: 10.1021/acsami.8b19241
ACS Appl. Mater. Interfaces XXXX, XXX, XXX−XXX

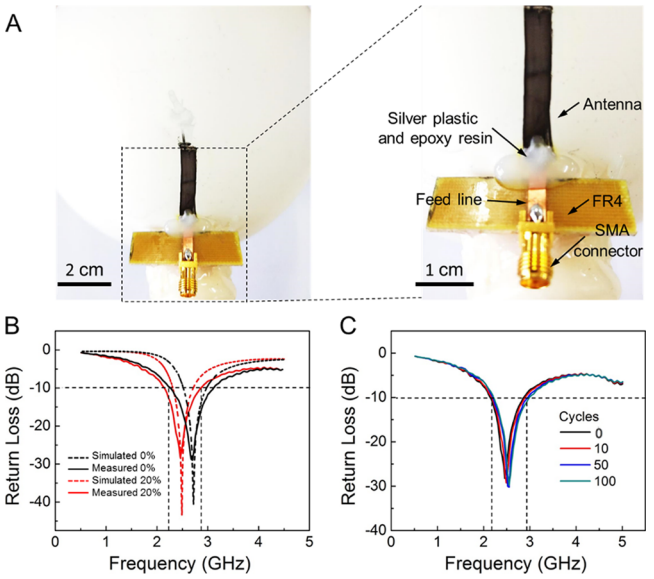

Figure 7. (A) Optical image of the $Ag_{24\ nm}$-$SACNS_1$/catheter monopole antenna with a glass epoxy panel (grade FR-4) and SMA connector attached. (B) Comparison of the measured (solid curves) and simulated (dashed curves) return loss for the $Ag_{24\ nm}$-$SACNS_1$/catheter monopole antenna at 0 and 20% strain. (C) Return loss of the $Ag_{24\ nm}$-$SACNS_1$/catheter monopole antenna for cyclic inflation/deflation tests. The omnidirectional fabrication strain is 80%.

frequency is 2.45 GHz, which is also close to the simulation value of 2.49 GHz. The measured peak return loss is −27.9 dB, corresponding to efficient transmission of over 99.99% power at the resonant frequency. The measured resonant frequencies agree well with the simulation results, with a slight difference due to the uncertainty in fabrication and characterization. The measured antenna bandwidths (frequency range for reflection loss is smaller than −10 dB) are 700 MHz (from 2.10 to 2.80 GHz) and 840 MHz (from 2.24 to 3.08 GHz) for the deflated and inflated states, respectively, indicating a reasonable working range for high-quality wireless communications. For reliable communication, it is essential that the antenna can survive multiple inflation/deflation cycles; thus, we tested it for 100 inflation/deflation cycles up to 20% biaxial strain. Figure 7C shows that the operation frequency and the return loss of the antenna almost remain unchanged after repeated inflation/deflation cycles, indicating the high robustness of our inflatable $Ag_{24\ nm}$-$SACNS_1$/catheter antenna.

In order to determine the ability of a monopole antenna of $Ag_{24\ nm}$-$SACNS_1$/catheter to transmit and receive signals after inflating or deflating, we composed a communication system operating at 2.45 GHz to receive or transmit signals in an open field based on the monopole antenna of $Ag_{24\ nm}$-$SACNS_1$/catheter. For this test, two antenna modules were used as the transmitter and receiver. One antenna module was integrated with the monopole antenna of $Ag_{24\ nm}$-$SACNS_1$/catheter, and the other one was integrated with a commercial monopole antenna. The maximum transmitted power of the antenna module is 7.0 dBm (5.0 mW), and the sensitivity of the receiver was −96.0 dBm. Figure 8A,B shows that the antenna signal (text message of "Nankai University") can be received or transmitted at a distance of 26.0 m when the monopole

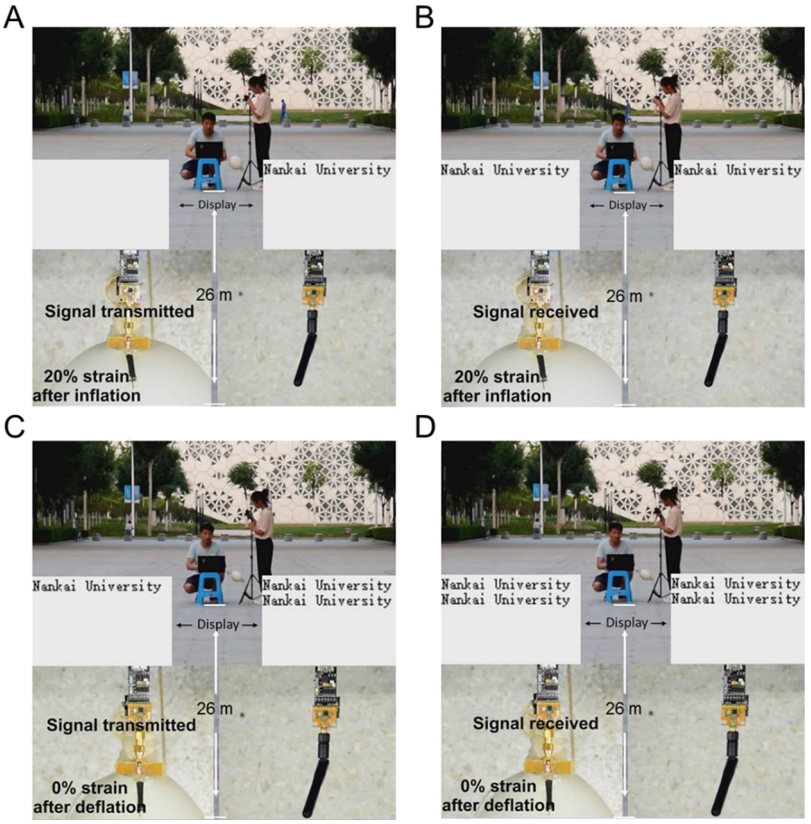

Figure 8. (A–D) Photographs showing (A, B) the antenna signal (text message of "Nankai University") that can be transmitted or received at a distance of 26.0 m when the monopole antenna of $Ag_{24\ nm}$-$SACNS_1$/catheter was inflated to 20% strain, and (C, D) as the $Ag_{24\ nm}$-$SACNS_1$/catheter was deflated to 0% strain, it communicated well with the transmitter and receiver for a distance of 26.0 m.

DOI: 10.1021/acsami.8b19241
ACS Appl. Mater. Interfaces XXXX, XXX, XXX−XXX

antenna of $Ag_{24\ nm}$-$SACNS_1$/catheter was inflated to 20% biaxial strain. As the monopole antenna was deflated to 0% strain, it communicated well with the transmitter and receiver for a distance of 26.0 m (Figure 8C,D and Movie S2). The wireless transmission may find applications in transferring different signals wirelessly, such as temperature, pressure, and biosignals (glucose, antibodies, etc.). The design without wires may decrease the risk of wire disconnection and simplify the device constructions by eliminating the transmission wires. Furthermore, if the inflation/deflation of the catheter and its movement can be controlled remotely by using wirelessly controlled actuators, then the wireless communication will be important in these scenarios.

In summary, we have demonstrated a straightforward scalable approach for fabrication of highly inflatable $SACNS_m$/catheter conducting devices with controllable two-dimensional buckled structures including quasi-parallel buckles, crisscrossed buckles, and hierarchically buckled structures by coating SACNS on the pre-inflated catheter, which enabled reversible inflation/deflation for up to 7470% volumetirc strain. The hierarchically buckled $SACNS_m$/catheter showed stable electrical resistance and tunable surface wetting properties. Such structures could be patterned by lithographic techniques and broaden the design options of functional devices. We also demonstrated inflatable tumor ablation devices, capacitive volumetric sensors, and inflatable antennas using SACNS-coated catheter devices. The presently demonstrated inflatable $SACNS_m$/catheter devices open new avenues for inflatable electronics such as space exploration and medical applications.

EXPERIMENTAL SECTION

Fabrication of $SACNS_m$/Catheter and $SACNS_m$/Catheter/$SACNS_m$. The process for making a $SACNS_m$/catheter is described in the following. First, a catheter was inflated to a fabrication strain using an air pump. Freestanding SACNS films were attached over the inflated catheter and densified with ethanol (98%) on the catheter surface. After ethanol drying, the inflated catheter was slowly deflated to form a $SACNS_m$/catheter. To prepare a $SACNS_m$/catheter/$SACNS_m$, a deflated $SACNS_m$/catheter was inflated again to the fabrication strain, and then, another layer of $SACNS_m$ was applied on the eversion of the inflated $SACNS_m$/catheter surface. After densification using ethanol (98%), the catheter was deflated to form a $SACNS_m$/catheter/$SACNS_m$.

Microscopy, Widths of Buckles and Islands, Resistance, Strain, Contact Angle, IR Thermal Images, Volume, and Capacitance Measurements. A field-emission scanning electron microscope (model Nova NanoSEM450) was used to obtain SEM images. The resistance of $SACNS_m$/catheter was measured using a Keithley 2400 SourceMeter unit via a two-probe method. The strain of an inflated catheter was measured by measuring the length between the two points on the catheter using a soft ruler, which were drawn on the inflated catheter. The average widths of the SACNS buckles and islands were measured with SEM images, which are taken from samples with the same preparation conditions of five different batches. Contact angle measurements were conducted by taking photos using a camera at ambient temperature. An infrared (IR) thermometer (FLIR T440) was used to obtain thermal IR images and temperatures. The average temperature of the catheter surface was obtained by using the "average function" in FLIR software. Actual volume of the inflated catheter was measured using water displacement in a partially water-filled tank, which acted as a plethysmograph to provide a measure of actual catheter volume. A capacitance meter (BK precision 810C) was used to measure the capacitance.

Cell Culture and Toxicity Assay. The mouse myoblast C2C12 cells were purchased from the Cell Bank of the Shanghai Institute of Biochemistry and Cell Biology at the Chinese Academy of Sciences (Shanghai, China). C2C12 cells were cultured in DMEM media. The media were supplemented with 10% fetal bovine serum, 50 μg/mL penicillin, and 50 μg/mL streptomycin at 37 °C and 5% CO_2 in a humidified environment.

The cell viability of C2C12 cells, measured by 3-(4,5-dimethylthiazol-2-yl)-2,5-diphenyltetrazolium bromide (MTT) assay, was used as an indicator to evaluate the toxicity of SACNS. SACNS was stacked to the bottom of 96-well culture plates. The cells were plated on the SACNS (5×10^3 cells/well). After incubation for 24, 48, or 72 h, 20 μL of MTT (5 mg/mL) was added to each well. The formed formazan crystals were dissolved in DMSO (150 μL/well) by constant shaking for 10 min. The absorbance was measured on an ELISA reader (SpectraMax Plus384, Molecular Devices, Sunnyvale, CA) at a test wavelength of 570 nm and a reference wavelength of 630 nm. Cell viability was calculated using the following formula: % cell viability = $A_t/A_s \times 100\%$, where A_t and A_s denote the absorbance of the SACNS and media control, respectively.

Simulation, Fabrication, and Measurements of the Monopole Ag_t-$SACNS_m$/Catheter Antenna. The conducting electrodes used to fabricate the antenna were silver-coated SACNS (Ag_t-SACNS). First, we deposited a thin layer of silver on SACNS to improve its conductivity using an FJL-560C series magnetron sputtering system. Then, the Ag_t-$SACNS_m$/catheter was fabricated using a similar process for preparing $SACNS_m$/catheters by replacing m layers of SACNS with m layers of Ag_t-SACNS. $Ag_{24\ nm}$-SACNS films were obtained by using the power at 14.0 W for 8 min, and the fabrication strain of $Ag_{24\ nm}$-$SACNS_1$/catheter was 80%. To obtain the desired resonant frequency and impedance, a commercial code ANSYS high-frequency structure simulator (HFSS) was used for calculating the required length and width of the inflatable antenna. For a resonant frequency of 2.45 GHz, the simulated values for the length and width of the antenna are 28.0 and 6.0 mm, respectively. Because the antenna size was relatively small, a tiny fabrication error may result in a non-negligible shift in operation frequency. Therefore, several parallel antennas of the same specifications were prepared. For excitation measurements of the antenna, a microstrip feed line having an impedance of 50 Ω on a flame resistant-4 (FR-4) board was connected to the antenna. The FR-4 board was used for holding the feed line and for the convenience of measurements. A 3.5 mm SubMiniature version A (SMA) connector was soldered to the substrate and connected to the feed line, with the connector body grounded. The feed line was attached to the center rectangle using silver paste to ensure good electrical contact between the $Ag_{24\ nm}$-SACNS and the feed line. The reflection loss of the antenna was measured using an Agilent E8363C 10 MHz ~40 GHz network analyzer.

In Vivo Antitumor Efficacy of $SACNS_m$/Catheter-Mediated Electrical Thermal Treatment. The C57BL/6 mice (female, 5 weeks old) with subcutaneously xenografted Hepa1-6 tumor were randomly divided into two groups (n = 3 per group). For the treatment group, $SACNS_m$/catheter was used as an inflatable tumor ablation to parcel the tumor in mouse, and then, electricity was turned on with a voltage of 20 V for 30 min. The IR thermal imaging camera (FLIR Corporation, USA) was used to monitor the heating effect of the treatment. The tumor volumes and body weights of two groups of mice were measured every 2 days for 16 consecutive days. During the period of treatment, iodophor and merbromin were used to sterilize the tumor foci and promote the scab off.

ASSOCIATED CONTENT

Supporting Information

The Supporting Information is available free of charge on the ACS Publications website at DOI: 10.1021/acsami.8b19241.

Discussions, tables, additional figures, and supplementary movies (PDF)

IR video of an inflated tubular $SACNS_5$/catheter tumor ablation device (MP4)

DOI: 10.1021/acsami.8b19241
ACS Appl. Mater. Interfaces XXXX, XXX, XXX−XXX

Demonstration of $Ag_{24\ nm}$-SACNS1/catheter monopole antenna applied to transmit and receive signals after inflating or deflating (MP4)

AUTHOR INFORMATION

Corresponding Author

*E-mail: liuzunfeng@nankai.edu.cn.

ORCID

Shougen Yin: 0000-0001-7337-2479
Weichao Wang: 0000-0001-5931-212X
Yinsong Wang: 0000-0002-1403-2113
Zunfeng Liu: 0000-0002-7366-0275

Author Contributions

#R.W., Z.L., and G.W. contributed equally to this work.

Author Contributions

The manuscript was written through contributions of all authors. All authors have given approval to the final version of the manuscript.

Notes

The authors declare no competing financial interest.

ACKNOWLEDGMENTS

This work was supported by the National Key Research and Development Program of China (2017YFB0307000), the National Natural Science Foundation of China (grants U1533122, 51773094, and 8187141913), the Natural Science Foundation of Tianjin (grant number 18JCZDJC36800), the Science Foundation for Distinguished Young Scholars of Tianjin (grant number 18JCJQJC46600), the Fundamental Research Funds for the Central Universities (63171219), the Science and Technology Support Program of Changzhou (CZ20170007), the State Key Laboratory for Modification of Chemical Fibers and Polymer Materials, Donghua University (LK1704), and the National Science Foundation (grants CMMI-1661246, CMMI-1636306, and CMMI-1726435).

REFERENCES

(1) Sharon, E.; Roman, B.; Swinney, H. L. Geometrically Driven Wrinkling Observed in Free Plastic Sheets and Leaves. *Phys. Rev. E* **2007**, *75*, No. 046211.

(2) Chen, X.; Yin, J. Buckling Patterns of Thin Films on Curved Compliant Substrates with Applications to Morphogenesis and Three-Dimensional Micro-Fabrication. *Soft Matter* **2010**, *6*, 5667−5680.

(3) Liu, Z.; Swaddiwudhipong, S.; Hong, W. Pattern Formation in Plants Via Instability Theory of Hydrogels. *Soft Matter* **2013**, *9*, 577−587.

(4) Sharon, E.; Marder, M.; Swinney, H. L. Leaves, Flowers and Garbage Bags: Making Waves. *Am. Sci.* **2004**, *92*, 254−261.

(5) Liu, Z. F.; Fang, S.; Moura, F. A.; Ding, J. N.; Jiang, N.; Di, J.; Zhang, M.; Lepró, X.; Galvão, D. S.; Haines, C. S.; Yuan, N. Y.; Yin, S. G.; Lee, D. W.; Wang, R.; Wang, H. Y.; Lv, W.; Dong, C.; Zhang, R. C.; Chen, M. J.; Yin, Q.; Chong, Y. T.; Zhang, R.; Wang, X.; Lima, M. D.; Ovalle-Robles, R.; Qian, D.; Lu, H.; Baughman, R. H. Hierarchically Buckled Sheath-Core Fibers for Superelastic Electronics, Sensors, And Muscles. *Science* **2015**, *349*, 400−404.

(6) Efimenko, K.; Rackaitis, M.; Manias, E.; Vaziri, A.; Mahadevan, L.; Genzer, J. Nested Self-Similar Wrinkling Patterns in Skins. *Nat. Mater.* **2005**, *4*, 293−297.

(7) Kim, P.; Abkarian, M.; Stone, H. A. Hierarchical Folding of Elastic Membranes Under Biaxial Compressive Stress. *Nat. Mater.* **2011**, *10*, 952−957.

(8) Zang, J.; Ryu, S.; Pugno, N.; Wang, Q.; Tu, Q.; Buehler, M. J.; Zhao, X. Multifunctionality and Control of The Crumpling and Unfolding of Large-Area Graphene. *Nat. Mater.* **2013**, *12*, 321−325.

(9) Cao, C.; Chan, H. F.; Zang, J.; Leong, K. W.; Zhao, X. Harnessing Localized Ridges for High-Aspect-Ratio Hierarchical Patterns with Dynamic Tunability and Multifunctionality. *Adv. Mater.* **2014**, *26*, 1763−1770.

(10) Li, L.; Bai, Y.; Li, L.; Wang, S.; Zhang, T. A Superhydrophobic Smart Coating for Flexible and Wearable Sensing Electronics. *Adv. Mater.* **2017**, *29*, 1702517.

(11) Su, Y.; Ping, X.; Yu, K. J.; Lee, J. W.; Fan, J. A.; Wang, B.; Li, M.; Li, R.; Harburg, D. V.; Huang, Y.; Yu, C.; Mao, S.; Shim, J.; Yang, Q.; Lee, P. Y.; Armonas, A.; Choi, K.-J.; Yang, Y.; Paik, U.; Chang, T.; Dawidczyk, T. J.; Huang, Y.; Wang, S.; Rogers, J. A. In-Plane Deformation Mechanics for Highly Stretchable Electronics. *Adv. Mater.* **2017**, *29*, 1604989.

(12) Shen, J.; Seker, O.; Sutchiewcharn, N.; Akbas, B. Cyclic Behavior of Buckling-Controlled Braces. *J. Constr. Steel Res.* **2016**, *121*, 110−125.

(13) Shen, J.; Seker, O.; Akbas, B.; Seker, P.; Momenzadeh, S.; Faytarouni, M. Seismic Performance of Concentrically Braced Frames with And Without Brace Buckling. *Eng. Struct.* **2017**, *141*, 461−481.

(14) Wang, R.; Jiang, N.; Su, J.; Yin, Q.; Zhang, Y.; Liu, Z.; Lin, H.; Moura, F. A.; Yuan, N.; Roth, S.; Rome, R. S.; Ovalle-Robles, R.; Inoue, K.; Yin, S.; Fang, S.; Wang, W.; Ding, J.; Shi, L.; Baughman, R. H.; Liu, Z. A Bi-Sheath Fiber Sensor for Giant Tensile and Torsional Displacements. *Adv. Funct. Mater.* **2017**, *27*, 1702134.

(15) Lacour, S. P.; Wagner, S.; Huang, Z.; Suo, Z. Stretchable Gold Conductors on Elastomeric Substrates. *Appl. Phys. Lett.* **2003**, *82*, 2404−2406.

(16) Tahk, D.; Lee, H. H.; Khang, D.-Y. Elastic Moduli of Organic Electronic Materials by the Buckling Method. *Macromolecules* **2009**, *42*, 7079−7083.

(17) Zhang, Z.; Deng, J.; Li, X.; Yang, Z.; He, S.; Chen, X.; Guan, G.; Ren, J.; Peng, H. Superelastic Supercapacitors with High Performances During Stretching. *Adv. Mater.* **2015**, *27*, 356−362.

(18) Oyewole, O. K.; Yu, D.; Du, J.; Asare, J.; Oyewole, D. O.; Anye, V. C.; Fashina, A.; Zebaze Kana, M. G.; Soboyejo, W. O. Micro-Wrinkling and Delamination-Induced Buckling of Stretchable Electronic Structures. *J. Appl. Phys.* **2015**, *117*, 235501.

(19) Vandeparre, H.; Desbief, S.; Lazzaroni, R.; Gay, C.; Damman, P. Confined Wrinkling: Impact on Pattern Morphology and Periodicity. *Soft Matter* **2011**, *7*, 6878−6882.

(20) Görrn, P.; Cao, W.; Wagner, S. Isotropically Stretchable Gold Conductors on Elastomeric Substrates. *Soft Matter* **2011**, *7*, 7177−7180.

(21) Yu, J.; Lu, W.; Pei, S.; Gong, K.; Wang, L.; Meng, L.; Huang, Y.; Smith, J. P.; Booksh, K. S.; Li, Q.; Byun, J.-H.; Oh, Y.; Yan, Y.; Chou, T.-W. Omnidirectionally Stretchable High-Performance Supercapacitor Based on Isotropic Buckled Carbon Nanotube Films. *ACS Nano* **2016**, *10*, 5204−5211.

(22) Reiter, G. Dewetting of Thin Polymer Films. *Phys. Rev. Lett.* **1992**, *68*, 75−78.

(23) Yamaguchi, T.; Suematsu, N.; Mahara, H. Self-Organization of Hierarchy: Dissipative-Structure Assisted Self-Assembly of Metal Nanoparticles in Polymer Matrices. In *Nonlinear Dynamics in Polymeric Systems*; Pojman, J. A., Tran-Cong-Miyata, Q., Eds.; ACS Publications: ACS Symposium Series; 2003.

(24) Liu, G.; Ding, J. Diblock Thin Films with Densely Hexagonally Packed Nanochannels. *Adv. Mater.* **1998**, *10*, 69−71.

(25) Bowden, N.; Brittain, S.; Evans, A. G.; Hutchinson, J. W.; Whitesides, G. M. Spontaneous Formation of Ordered Structures in Thin Films of Metals Supported on An Elastomeric Polymer. *Nature* **1998**, *393*, 146−149.

(26) Ohzono, T.; Matsushita, S. I.; Shimomura, M. Coupling of Wrinkle Patterns to Microsphere-Array Lithographic Patterns. *Soft Matter* **2005**, *1*, 227−230.

(27) Chan, E. P.; Crosby, A. J. Spontaneous Formation of Stable Aligned Wrinkling Patterns. *Soft Matter* **2006**, *2*, 324−328.

DOI: 10.1021/acsami.8b19241
ACS Appl. Mater. Interfaces XXXX, XXX, XXX−XXX

(28) Huntington, M. D.; Engel, C. J.; Odom, T. W. Controlling the Orientation of Nanowrinkles And Nanofolds By Patterning Strain in A Thin Skin Layer on A Polymer Substrate. *Angew. Chem., Int. Ed.* **2014**, *126*, 8255−8259.
(29) Schweikart, A.; Horn, A.; Böker, A.; Fery, A. Controlled Wrinkling as A Novel Method for The Fabrication of Patterned Surfaces. In *Complex Macromolecular Systems I*; Springer: Berlin, Heidelberg, 2009; Vol. *227*, pp 75-99.
(30) Zhang, M.; Fang, S.; Zakhidov, A. A.; Lee, S. B.; Aliev, A. E.; Williams, C. D.; Atkinson, K. R.; Baughman, R. H. Strong, Transparent, Multifunctional, Carbon Nanotube Sheets. *Science* **2005**, *309*, 1215−1219.
(31) Lima, M. D.; Fang, S.; Lepró, X.; Lewis, C.; Ovalle-Robles, R.; Carretero-González, J.; Castillo-Martínez, E.; Kozlov, M. E.; Oh, J.; Rawat, N.; Haines, C. S.; Haque, M. H.; Aare, V.; Stoughton, S.; Zakhidov, A. A.; Baughman, R. H. Biscrolling Nanotube Sheets and Functional Guests into Yarns. *Science* **2011**, *331*, 51−55.
(32) Niu, Z.; Dong, H.; Zhu, B.; Li, J.; Hng, H. H.; Zhou, W.; Chen, X.; Xie, S. Highly Stretchable, Integrated Supercapacitors Based on Single-Walled Carbon Nanotube Films with Continuous Reticulate Architecture. *Adv. Mater.* **2013**, *25*, 1058−1064.
(33) Chen, X.; Lin, H.; Chen, P.; Guan, G.; Deng, J.; Peng, H. Smart, Stretchable Supercapacitors. *Adv. Mater.* **2014**, *26*, 4444−4449.
(34) Wang, H.; Liu, Z.; Ding, J.; Lepró, X.; Fang, S.; Jiang, N.; Yuan, N.; Wang, R.; Yin, Q.; Lv, W.; Liu, Z.; Zhang, M.; Ovalle-Robles, R.; Inoue, K.; Yin, S.; Baughman, R. H. Downsized Sheath-Core Conducting Fibers for Weavable Superelastic Wires, Biosensors, Supercapacitors, and Strain Sensors. *Adv. Mater.* **2016**, *28*, 4998−5007.
(35) Lv, W.; Jiang, N.; Ding, J.; Liu, Z.; Yuan, N.; Ovalle-Robles, R.; Inoue, K.; Lepró, X.; Fang, S. Three-Dimensional Conducting Elastomeric Composites Based on Buckling Carbon Nanotube Sheets for Interconnects and Temperature Sensor. *J. Nanosci. Nanotechnol.* **2017**, *17*, 1934−1941.
(36) Xu, F.; Wang, X.; Zhu, Y.; Zhu, Y. Wavy Ribbons of Carbon Nanotubes for Stretchable Conductors. *Adv. Funct. Mater.* **2012**, *22*, 1279−1283.
(37) Choi, C.; Lee, J. M.; Kim, S. H.; Kim, S. J.; Di, J.; Baughman, R. H. Twistable and Stretchable Sandwich Structured Fiber for Wearable Sensors and Supercapacitors. *Nano Lett.* **2016**, *16*, 7677−7684.
(38) Mu, J.; Hou, C.; Wang, G.; Wang, X.; Zhang, Q.; Li, Y.; Wang, H.; Zhu, M. An Elastic Transparent Conductor Based on Hierarchically Wrinkled Reduced Graphene Oxide for Artificial Muscles and Sensors. *Adv. Mater.* **2016**, *28*, 9491−9497.
(39) Dewire, J.; Calkins, H. State-of-the-Art and Emerging Technologies for Atrial Fibrillation Ablation. *Nat. Rev. Cardiol.* **2010**, *7*, 129−138.
(40) Tan, Y.; Chu, Z.; Jiang, Z.; Hu, T.; Li, G.; Song, J. Gyrification-Inspired Highly Convoluted Graphene Oxide Patterns for Ultralarge Deforming Actuators. *ACS Nano* **2017**, *11*, 6843−6852.
(41) Dinyari, R.; Rim, S. B.; Huang, K.; Catrysse, P. B.; Peumans, P. Curving Monolithic Silicon for Nonplanar Focal Plane Array Applications. *Appl. Phys. Lett.* **2008**, *92*, 091114.
(42) Huang, Z. Y.; Hong, W.; Suo, Z. Nonlinear Analyses of Wrinkles in A Film Bonded to A Compliant Substrate. *J. Mech. Phys. Solids* **2005**, *53*, 2101−2118.
(43) Yin, J.; Yagüe, J. L.; Eggenspieler, D.; Gleason, K. K.; Boyce, M. C. Deterministic Order in Surface Micro-Topologies through Sequential Wrinkling. *Adv. Mater.* **2012**, *24*, 5441−5446.
(44) Cao, Y.; Hutchinson, J. W. Wrinkling Phenomena in Neo-Hookean Film/Substrate Bilayers. *J. Appl. Mech.* **2012**, *79*, 031019.
(45) Chen, X.; Hutchinson, J. W. Herringbone Buckling Patterns of Compressed Thin Films on Compliant Substrates. *J. Appl. Mech.* **2004**, *71*, 597−603.
(46) Im, S. H.; Huang, R. Wrinkle Patterns of Anisotropic Crystal Films on Viscoelastic Substrates. *J. Mech. Phys. Solids* **2008**, *56*, 3315−3330.
(47) Lipomi, D. J.; Vosgueritchian, M.; Tee, B. C.-K.; Hellstrom, S. L.; Lee, J. A.; Fox, C. H.; Bao, Z. Skin-Like Pressure and Strain Sensors Based on Transparent Elastic Films of Carbon Nanotubes. *Nat. Nanotechnol.* **2011**, *6*, 788−792.
(48) Chen, Z.; Ren, W.; Gao, L.; Liu, B.; Pei, S.; Cheng, H.-M. Three-Dimensional Flexible and Conductive Interconnected Graphene Networks Grown by Chemical Vapour Deposition. *Nat. Mater.* **2011**, *10*, 424−428.
(49) Njoku, E. G.; Rahmat-Samii, Y.; Sercel, J.; Wilson, W. J.; Moghaddam, M. Evaluation of An Inflatable Antenna Concept for Microwave Sensing of Soil Moisture and Ocean Salinity. *IEEE Trans. Geosci. Remote Sens.* **1999**, *37*, 63−78.
(50) Huang, J. The development of inflatable array antennas. *IEEE Antennas Propag. Mag.* **2001**, *43*, 44−50.
(51) Neufeld, D. M.; Shemesh, E. I.; Kodner, I. J.; Shatz, B. A. Endoscopic Management Of Anastomotic Colon Strictures With Electrocautery And Balloon Dilation. *Gastrointest. Endosc.* **1987**, *33*, 24−26.
(52) Nolan, T. D. C.; Hattler, B. G.; Federspiel, W. J. Development of a Balloon Volume Sensor for Pulsating Balloon Catheters. *ASAIO J.* **2004**, *50*, 225−233.
(53) Kim, D.-H.; Lu, N.; Ghaffari, R.; Kim, Y.-S.; Lee, S. P.; Xu, L.; Wu, J.; Kim, R.-H.; Song, J.; Liu, Z.; Viventi, J.; de Graff, B.; Elolampi, B.; Mansour, M.; Slepian, M. J.; Hwang, S.; Moss, J. D.; Won, S.-M.; Huang, Y.; Litt, B.; Rogers, J. A. Materials for Multifunctional Balloon Catheters with Capabilities in Cardiac Electrophysiological Mapping and Ablation Therapy. *Nat. Mater.* **2011**, *10*, 316−323.
(54) Chang, J. K.; Chung, S.; Lee, Y.; Park, J.; Lee, S.-K.; Yang, S. S.; Moon, S.-Y.; Han, D.-C. In Intravascular Micro Active Catheter for Minimal Invasive Surgery, *Microtechnologies in Medicine and Biology, 1st Annual International, Conference*, Lyon, France, Oct. 2000; IEEE: Lyon, France, 2000; pp 243-246.
(55) Chu, K. F.; Dupuy, D. E. Thermal Ablation of Tumours: Biological Mechanisms and Advances in Therapy. *Nat. Rev. Cancer* **2014**, *14*, 199−208.
(56) Liu, T.; Zhang, N.; Wang, Z.; Wu, M.; Chen, Y.; Ma, M.; Chen, H.; Shi, J. Endogenous Catalytic Generation of O_2 Bubbles for *In Situ* Ultrasound-Guided High Intensity Focused Ultrasound Ablation. *ACS Nano* **2017**, *11*, 9093−9102.
(57) Ma, M.; Xu, H.; Chen, H.; Jia, X.; Zhang, K.; Wang, Q.; Zheng, S.; Wu, R.; Yao, M.; Cai, X.; Li, F.; Shi, J. A Drug-Perfluorocarbon Nanoemulsion With an Ultrathin Silica Coating for The Synergistic Effect of Chemotherapy and Ablation by High-Intensity Focused Ultrasound. *Adv. Mater.* **2014**, *26*, 7378−7385.
(58) Wan, G.; Chen, B.; Li, L.; Wang, D.; Shi, S.; Zhang, T.; Wang, Y.; Zhang, L.; Wang, Y. Nanoscaled Red Blood Cells Facilitate Breast Cancer Treatment by Combining Photothermal/Photodynamic Therapy and Chemotherapy. *Biomaterials* **2018**, *155*, 25−40.
(59) Huang, W.; Huang, Y.; You, Y.; Nie, T.; Chen, T. High-Yield Synthesis of Multifunctional Tellurium Nanorods To Achieve Simultaneous Chemo-Photothermal Combination Cancer Therapy. *Adv. Funct. Mater.* **2017**, *27*, 1701388.

DOI: 10.1021/acsami.8b19241
ACS Appl. Mater. Interfaces XXXX, XXX, XXX−XXX